

How To Make A Thesis Following The Guideline With More Text To Have Two Lines



by

A Good Name

Submitted for the degree of

Doctor of Philosophy

SOME WEIRD INSTITUTE NO ONE EVER HEARD ABOUT

SCHOOL OF LATEX AND WRITING

HERIOT-WATT UNIVERSITY

September 2042

Abstract

In accordance with the Academic Regulations the thesis must contain an abstract preferably not exceeding 200 words, bound in to precede the thesis. The abstract should appear on its own, on a single page. The format should be the same as that of the main text. The abstract should provide a synopsis of the thesis and shall state clearly the nature and scope of the research undertaken and of the contribution made to the knowledge of the subject treated. There should be a brief statement of the method of investigation where appropriate, an outline of the major divisions or principal arguments of the work and a summary of any conclusions reached. The abstract must follow the Title Page.

Dedication

If a dedication is included then it should be immediately after the Abstract page.

I don't what it is actually.

Acknowledgements

I wanna thanks all coffee and tea manufacturers and sellers that made the completion of this work possible.

Contents

I	Chapters	1
1	Introduction	2
1.1	Cavitation	2
1.2	Comparison to Literature	13
2	Materials and Experimental Test Procedure	16
2.1	Experimental determination of SFE	16
2.2	Electrochemical measurement	17
2.3	Experimental electrochemical - polarize electrode to -1.5 to remove oxides	18
2.4	Description of constant phase element	18
2.5	Other stuff	18
2.6	Stellite 1	20
2.7	Stellites	21
2.8	Objectives and Scope of the Research Work	21
2.9	Thesis Outline	21
2.10	Literature Survey	21
2.11	Cavitation Tests	21
2.12	Charpy impact energy	21
3	Results and Analysis	22
3.1	Microstructure and Phase Analysis	22
3.2	Microstructure and Phase Analysis	22
3.3	Electrochemical corrosion tests	26
3.4	Strain hardening	26
4	Discussion	29
4.1	Experimental Test Procedure	29
4.1.1	Hardness Tests	29
4.1.2	Cavitation	29
4.2	Relationships between cavitation erosion resistance and mechanical properties	29
4.3	Influence of vibratory amplitude	29
4.4	Correlative empirical methods	30
5	Conclusions	32
II	Weird hanger-ons	33
6	Erosion particles	34
7	Reasons for why CE is less in seawater	35
8	Residual Stress and why it's important	36
9	Why HIP is better than cast	37
10	Equiaxed grains - why HIP is better than cast	38

11 Describing SEM images (light gray, dark, light)	39
12 Stellite 1	40
13 Parametric studies on Stellite	41
References	42

List of Tables

1.2	Cr ₃ C ₂	9
3.1	Microhardness HV _{0.01} of Al _{0.1} CoCrFeNi HEA [nairExceptionallyHighCavitation2018a]	27
3.2	Microhardness HV _{0.01} of 316LSS [nairExceptionallyHighCavitation2018a]	28

List of Figures

Glossary

BSE Backscatter Electrons.

EDX Energy-Dispersive X-ray.

FCC Face Centred Cubic.

HCP Hexagonal Close Packed.

HIP Hot Isostatically Pressed.

HV Hardness Vickers Scale.

PDF Powder Diffraction File.

SE Secondary Electrons.

SEM Scanning Electron Microscope/Microscopy.

XRD X-ray Diffraction.

Part I

Chapters

Chapter 1

Introduction

1. Mechanism of Cavitation-Induced Material Degradation

IGNORE_HEADING

1.1 Cavitation

IGNORE

Stellites are a family of cobalt-base superalloys used in aggressive service environments due to retention of strength, wear resistance, and oxidation resistance at high temperature [1, 2]. First developed in the early 1900s [3], stellites became critical to components used in medical implants & tools, machine tools, and nuclear components, with new variations on the original CoCrWC and CoCrMoC alloys seeing expanding use in sectors like oil & gas and chemical processing [1, 4, 5].

The main alloying elements in Stellite alloys are cobalt (Co), chromium (25-33 wt% Cr), tungsten (0-18 wt% W), molybdenum (0-18 wt% Mo), carbon (0.1-3.3 wt% C), and trace elements iron (Fe), nickel (Ni), silicon (Si), phosphorus (P), sulphur (S), boron (B), lanthanum (La), & manganese (Mn); Table 1.1 summarizes the nominal and measured composition of commonly used Stellite alloys [ahmedMappingMechanicalProperties2023, davis2000nickel, 6–13]. Stellite alloys possess a composite-like microstructure, combining a cobalt-rich matrix strengthened by solid solutions of chromium, tungsten, & molybdenum, with embedded hard carbide phases with carbide formers Cr (of carbide type M_7C_3 & $M_{23}C_6$) and W/Mo (of carbide type MC & M_6C), that impede wear and crack propagation [14, 15].

Understanding the cobalt phase is crucial for studying structural changes in Co-based alloys widely used in industry. The fcc cobalt phase, especially its delayed transition to hcp at ambient and moderate temperatures [DUBOS2020128812], is of particular interest due to its impact on material properties in Co-based alloys [Rajan19821161]. As the cobalt phase in stellite alloys is observed to consist of the fcc phase [Rajan19821161], the potential for strain-induced fcc to hcp transformation is of interest under the mechanical loading of cavitation erosion.

Cobalt exhibits a hexagonal close-packed (hcp) structure above 700 K ¹the theoretical transition temperature was determined to be 825 K by Lizarraga et al [Lizarraga2017]} and shifts to a face-centered cubic (fcc) structure above this temperature.

At ambient conditions, the metastable FCC retained phase can be transformed into HCP phase

¹{

																Chapter 1. Introduction
Alloy	Co	Cr	W	Mo	C	Fe	Ni	Si	P	S	B	La	Mn	Ref	Process	Type
Stellite 1	47.7	30	13	0.5	2.5	3	1.5	1.3					0.5	[davis2000nickel]		Nominal
	48.6	33	12.5	0	2.5	1	1	1.3					0.1	[6]		
	46.84	31.7	12.7	0.29	2.47	2.3	2.38	1.06					0.26	[ahmedMappingMechanicalProperties2023]	HIPed ^a	
Stellite 3	50.5	33	14		2.5									[8]		
	49.24	29.57	12.07	0.67	2.52	2.32	1.07	1.79					0.75	[12]	HIPed ^a	
Stellite 4	45.43	30	14	1	0.57	3	3	2					1	[davis2000nickel]		Nominal
	51.5	30	14		1	1	2	0.5						[13]		
	51.9	33	14		1.1									[8]		
	49.41	31	14	0.12	0.67	2.16	1.82	1.04					0.26	[ahmedMappingMechanicalProperties2023]	HIPed ^a	
	50.2	29.8	14.4	0	0.7	1.9	1.9	0.8					0.3	[7]	HIPed ^a	
Stellite 6	51.5	28.5	4.5	1.5	1	5	3	2			1		2	[davis2000nickel]		Nominal
	63.81	27.08	5.01		0.96	0.73	0.87	1.47					0.07	[12]	HIPed ^a	
	60.3	29	4.5		1.2	2	2	1						[13]		
	61.7	27.5	4.5	0.5	1.15	1.5	1.5	1.15					0.5	[8]		
	58.46	29.5	4.6	0.22	1.09	2.09	2.45	1.32					0.27	[ahmedMappingMechanicalProperties2023]	HIPed ^a	
	58.04	30.59	4.72		1.24	2.03	1.87	0.80	0.01	0.01				[10]	PTAW ^e	
	55.95	27.85	3.29		0.87	6.24	3.63	1.23	0.01	0.01			0.45	[10]	GTAW ^d	
	52.40	30.37	3.57		0.96	6.46	3.93	1.70	0.01	0.01			0.3	[10]	SMAW ^c	

	60.3		31.10	4.70	0.30	1.10	1.70	1.50	1.30	0.00	0.3	[11]	LP-DED	Chapter 1. Introduction
	60.6	27.7	5	0	1.2	1.9	2	1.3			0.3	[7]	HIPed ^a	
Stellite 12	53.6	30	8.3		1.4	3	1.5	0.7			1.5	[davis2000nickel]	Nominal	Introduction
	55.22	29.65	8.15	0.2	1.49	2.07	2.04	0.91			0.27	[ahmedMappingMechanicalProperties2023]	HIPed ^a	
Stellite 20	41.05	33	17.5		2.45	2.5	2.5				1	[davis2000nickel]	Nominal	Introduction
	43.19	31.85	16.3	0.27	2.35	2.5	2.28	1			0.26	[ahmedMappingMechanicalProperties2023]	HIPed ^a	
Stellite 21	59.493	27		5.5	0.25	3	2.75	1		0.007	1	[davis2000nickel]	Nominal	Introduction
	60.6	26.9	0	5.7	0.2	1.3	2.7	1.9			0.7	[7]	HIPed ^a	
Stellite 31	57.5	22	7.5		0.5	1.5	10	0.5			0.5	[davis2000nickel]	Nominal	Introduction
	52.9	25.3	7.8	0	0.5	1.1	11.4	0.6			0.4	[7]	HIPed ^a	
Stellite 190	46.7	27	14	1	3.3	3	3	1			1	[davis2000nickel]	Nominal	Introduction
	48.72	27.25	14.4	0.2	3.21	2.1	2.81	1			0.31	[ahmedMappingMechanicalProperties2023]	HIPed ^a	

by mechanical loading, although any HCP phase is completely transformed into a FCC phase between 673 K and 743 K [DUBOS2020128812].

The main allotropes of the Co solid solution in stellite are the hexagonal close-packed (hcp) ϵ Co (ICDD# 01-071-4239) and the face-centered cubic (fcc) γ Co (ICDD 00-015-0806) [16] with the ϵ Co phase being more thermodynamically stable below 700K [17]. However the $\gamma \rightarrow \epsilon$ transformation is difficult to achieve under normal condition, leading to cobalt alloys often retaining the metastable γ phase [davis2000nickel, 18]. At ambient conditions, the metastable fcc retained phase in stellites can undergo a strain-induced martensitic-type transition involving partial dislocation movement [HUANG2023106170], such as during cavitation erosion as observed experimentally by Woodford [19].

The fcc to hcp transition is related to the very low stacking fault energy of the fcc structure (7 mJ/m²) of cobalt [Tawancy1986337]

This promotes the FCC \rightarrow HCP martensitic transformation and improves the mechanical properties of the alloy. Phase composition seriously affects the properties of alloys. The FCC phase is soft and plastic, while the HCP phase is hard and not plastic. Therefore, when an alloy undergoes strain-induced FCC \rightarrow HCP martensitic transformation, the martensite HCP phase plays a “secondary hardening” effect, which greatly improves the overall hardness of the alloy.

This fcc to hcp transition is linked to the very low stacking fault energy of the fcc structure (approximately 7 mJ/m²). The addition of other elements influences these characteristics: solid-solution strengthening increases the fcc cobalt matrix strength by distorting the atomic lattice and can decrease the low stacking fault energy by adjusting the electronic structure. Solute atoms like molybdenum (Mo) and tungsten (W), due to their large atomic sizes, discourage dislocation motion in stellites. Since dislocation cross-slip is a primary deformation mode in imperfect crystals at elevated temperatures and dislocation slip is a diffusion-enhanced process at high temperatures, this contributes to high-temperature stability. Furthermore, elements like nickel (Ni), iron (Fe), and carbon (C) stabilize the fcc structure of cobalt ($a = 0.35$ nm), while chromium (Cr) and tungsten (W) tend to stabilize the hcp structure ($a = 0.25$ nm and $c = 0.41$ nm).

The ϵ – Co (ICDD# 01-071-4239) and γ – Co (ICDD 00-015-0806) phases are the main phases of the Co solid solution in stellite. Although the ϵ – Co phase is more stable at room temperature according to the phase diagram, cobalt alloys often possess a majority γ – Co phase; the $\gamma \rightarrow \epsilon$ transformation rarely occurs under normal cooling conditions and the metastable γ phase is generally retained.

Cobalt and Co-Cr alloys undergo thermally induced phase transformation from the high temperature face-centered cubic (fcc) γ phase to low temperature hexagonal close-packed (hcp) ϵ phase at 700 K and strain induced fcc-hcp transition through martensitic-type mechanism (partial movement of dislocations) [HUANG2023106170]. At ambient conditions, the metastable

FCC retained phase in stellites can be transformed into HCP phase by mechanical loading, although any HCP phase is completely transformed into a FCC phase between 673 K and 743 K [DUBOS2020128812]; the metastable fcc cobalt phase in stellite alloys [Rajan19821161] absorbs a large part of imparted energy under the mechanical loading of cavitation erosion. The fcc to hcp transition is related to the very low stacking fault energy of the fcc structure (7 mJ/m²) [Tawancy1986337].

Solid-solution strengthening leads to increase of the fcc cobalt matrix strength (due to distortion of the atomic lattice with the addition of elements of different atomic radii), and decrease of low stacking fault energy [Tawancy1986337] due to the adjusted electronic structure of the metallic lattice. Dislocation motion in stellites is discouraged by solute atoms of Mo and W, due to the large atomic sizes. Given that dislocation cross slip is the main deformation mode in imperfect crystals at elevated temperature, as dislocation slip is a diffusion process that is enhanced at high temperature, this leads to high temperature stability [LIU2022294]. In addition, nickel (Ni), iron (Fe), and carbon (C) stabilize the fcc structure of cobalt ($a = 0.35$ nm), while chromium (Cr) and tungsten (W), stabilize the hcp structure ($a = 0.25$ nm and $c = 0.41$ nm) [Vacchieri20171100, Tawancy1986337].

[19]

confirmed that $\gamma \rightarrow \epsilon$ transformation occur on the surface of cobalt-base alloys during cavitation erosion, a relationship a direct relationship between . While the extent of this deformation-induced transformation was observed to increase with the severity of erosion and reach a steady state corresponding with the weight loss rate, subsequent experiments on Stellite 6B with varying initial hcp phase content and different aging treatments failed to establish a direct correlation between the transformation characteristics and erosion resistance.

Solid-solution strengthening is provided by elements not tied in secondary phases, leading to increase of the fcc cobalt matrix strength.

With the addition of elements with different atomic radiuses, the atomic lattice of the fcc cobalt matrix is distorted leading to increased strength. The already low stacking fault energy of the fcc cobalt structure (7 mJ/m²) [Tawancy1986337] is further decreased, inhibiting dislocation cross slip. Given that dislocation cross slip is the main deformation mode in imperfect crystals at elevated temperature, as dislocation slip is a diffusion process that is enhanced at high temperature, this leads to high temperature stability [LIU2022294].

The addition of nickel (Ni), iron (Fe), and carbon (C) stabilize the fcc structure of cobalt, while chromium (Cr) and tungsten (W), stabilize the hcp structure. Cr guarantees hot corrosion resistance and forms M₂₃C₆ carbides, while form MC carbides [Vacchieri20171100]. The fcc cobalt phase has lattice constant $a = 0.35$ nm while the hcp cobalt phase has lattice constant $a = 0.25$ nm and $c = 0.41$ nm [Tawancy1986337].

1. Paragraph: Other Elements

IGNORE

In Co based superalloys, Ni element is added in order to stabilize the fcc crystalline structure from room temperature to the melting temperature. It is also known that Fe also stabilises the fcc structure like Ni [24]. According to images of the elemental mapping analysis of Ni and Fe, they exhibited a homogenous distribution within the matrix.

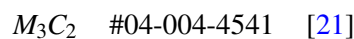
In the elemental mapping analysis, the amount of oxygen element increased significantly in the precipitates stated as M₂₃C₆ type carbides. It was reported that M₇C₃ and MC type carbides preferentially oxidized when exposed to high temperature [37]. Similarly, it was understood in the present study that M₂₃C₆ type carbides also oxidized during the sintering process.

The proportion and type of carbides depend on carbon content and the relative amounts of carbon with carbide formers (Cr, W, Mo), which greatly influence alloy performance and intended applications as carbides provide higher strength and but may reduce corrosion resistance due to localized corrosion at carbide boundaries. High carbon alloy (>1.2 wt%) have higher hardness due to greater carbide formation and are primarily used for wear resistance, low carbon alloys (<0.5 wt%) are used for enhanced corrosion resistance, and medium carbon alloys (0.5 wt% - 1.2 wt%) are used in applications requiring a combination of wear and corrosion resistance [davis2000nickel].

The carbide and grain size can be controlled by the rate of freezing, with larger carbide sizes indicating slower freezing rates [20].

The strength of most cobalt base superalloys is derived from the carbide phases present in the matrix and distributed around the grain boundaries. The carbides that form depend on the composition and thermal history of the material. The carbide former elements are from group IV (Ti, Zr, Hf), group V (Cb, Ta), and group VI (Cr, Mo, W). The types of carbides that are formed are as follows (M and C represents metal and carbon atoms respectively):

The types of chromium carbides formed, in order of increasing Cr/C ratio, are:



Phase	Cr_3C_2	$Cr_{23}C_6$
ICDD	#04-004-4541	
Crystal system	Orthorhombic	Cubic
Space group	Pnam (62)	Fm3m (225)
Pearson symbol	oP20	cF116
CAS	12012-05-0	12105-81-6

[22]

M 7 C3 : trigonal, a high chromium content carbide which forms at a slightly higher Cr/C ratio; M 23 C6 : cubic, a high chromium content carbide which forms at an higher Cr/C ratio, when the Cr is greater than 5 wt% of the alloy;

M6 C: complex cubic, a carbide phase whose volume fraction increases as refractory metals are introduced; MC: fcc NaCl structure, a carbide comprising metal groups IV and VI.

These carbides are listed above in the order of increasing stability, or free energy of formation. The stronger the carbide formers used, the greater is the tendency to form M6 C and MC carbides. The type of carbides that form is dependent upon both thermal history and composition.

2. Chromium carbide

3. Paragraph: Tungsten and Molybdenum carbides

Tungsten (W) and molybdenum (Mo) are refractory elements that provide solid solution strengthening to the matrix, by virtue of their large atomic size that impedes dislocation flow when present as solute atoms [**boeckRelationshipsProcessingMicrostructure1985**], and also form M_6C and $M_{12}C$ carbides along with MC carbides and Co_3M & Co_7M_6 intermetallics during solidification.

In carbon-rich regions, the MC phase (of type WC and MoC) is observed [23], which ca

In carbon-poor regions, ternary M_6C and $M_{12}C$ carbides have been identified, where the M_6C carbide (of type Co_3Mo_3C) is stable in the temperature ranges of 900C to 1300C and can vary in composition from $Mo_{40}Co_{46}C_{14}$ to $Mo_{56}Co_{30}C_{14}$, while the $Mo_{12}C$ carbide of type (Co_6Mo_6C carbide decomposes into Mo_6C and $\mu - Mo$ phases above 1100C [24].

When present in large quantities, W and Mo also participate in formation of W-rich or Mo-rich carbides during alloy solidification [**davis2000nickel**, 5],

leading to generation of Topologically Close-Packed (TCP) phases, such as the μ phase (of type Co_7W_6 and Co_7Mo_6) and σ phase (pf type Co_3W and Co_3Mo) [23], which are intermetallic brittle phases that add strength to the material [**ishidaIntermetallicCompoundsCobase2008**, 25] while also promoting crack initiation and propagation [26]. Previous work on the Stellite 1 sample by Ahmed et al [**ahmedMappingMechanicalProperties2023**] indicate that Co_6W_6C is identified as the main W-rich carbide in Stellite 1, although Co_3W_3C was also identified in addition to Co_3W and Co_7W intermetallics.

There are two main phases in the tungsten-carbon system: the hexagonal monocarbide WC (ICDD Card# 03-065-4539, COD:2102265), denoted as $\delta - WC$, and multiple variations

Table 1.2: Cr3C2

d(A)	Irel	h	k	l	2 θ
4.978	1L	1	1	0	17.804
3.983	1L	1	2	0	22.302
3.146	2	1	3	0	28.343
2.7460	18	0	1	1	32.582
2.5478	23	1	4	0	35.196
2.4897	13	2	2	0	36.045
2.4596	9	1	1	1	36.502
2.3063	100	1	2	1	39.023
2.2751	10	0	3	1	39.580
2.2409	60	2	3	0	40.210
2.1215	21	1	5	0	42.580
2.1036	10	1	3	1	42.961
1.9912	25	2	4	0	45.518
1.9481	45	2	1	1	46.582
1.9151	29	0	6	0	47.434
1.8934	34	1	4	1	48.011
1.8691	49	2	2	1	48.676
1.8190	27	3	1	0	50.107
1.7833	26	0	5	1	51.182
1.7670	1	2	5	0	51.691
1.7567	8	2	3	1	52.016
1.6975	25	1	5	1	53.972
1.6602	3	3	3	0	55.289
1.6285	6	2	4	1	56.458
1.5734	5	1	7	0+	58.625
1.5302	9	3	1	1	60.450
1.4987	7	2	5	1	61.858
1.4375	3	3	5	0	54.803
1.4192	3	0	7	1	65.742
1.4143	19	0	0	2	66.004
1.3902	1	1	8	0	67.298
1.3720	5	4	1	0	68.313
1.3273	4	3	6	0	70.951
1.2998	1	4	3	0	72.691
1.2812	2	3	5	1	73.916
1.2626	5	2	7	1	75.192
1.2474	13	1	8	1	76.268
1.2367	5	1	4	2	77.054
1.2342	6	4	1	1	77.234
1.2296	3	2	2	2	77.581
1.2254	8	3	7	0	77.896
1.2135	6	4	2	1	78.806
1.2017	11	3	6	1	79.731
1.1961	12	2	3	2	80.184
1.1810	10	4	3	1	81.421
1.1768	6	1	5	2	81.778
1.1619	6	2	8	1	83.056
1.1590	6	2	9	0	83.303
1.1531	8	2	4	2	83.832
1.1397	4	4	4	1	85.042
1.1377	11	0	6	2	85.225
1.1247	8	1	10	0+	86.451

of hexagonal-close-packed subcarbide W_2C (ICDD:00-002-1134, COD:1539792) [27, 28]

WC carbides precipitate as discrete particles distributed heterogeneously throughout the alloy intragranularly

The precipitation of the tungsten-rich phase M_6C is closely related to the decomposition of the MC carbide, and the M_6C only occurs in the vicinity of the MC [29], as M_6C carbides form only when the tungsten and/or molybdenum content exceeds 4-6 at. %.

Plasma nitrided Stellite 6 and 12 were found to have lowered corrosion resistance due to the consumption of chromium in CrN precipitates and lack of chromium oxide as protective layer [30].

The predominant carbide found in high-carbon Stellite is chromium rich Cr_7C_3 type whereas carbides such as Cr_6C and $Cr_{23}C_6$ are found in low-carbon Stellite. These carbides have a very high hardness (i.e. more than 1000 HV) and are responsible for imparting hardness to coating of Stellite thus improving its sliding wear resistance.

Chromium carbides have high hardness and wear resistance, as well as excellent resistance to chemical corrosion, making them often used in surface coatings [31]

In the Cr-C binary phase diagram, there are three phases : cubic $Cr_{23}C_6$ (space group , melting point 1848 K), orthorhombic Cr_3C_2 (space group Pnma, melting point 2083 K) and Cr_7C_3 (space group Pnma, melting point 2038 K) [32] [31]

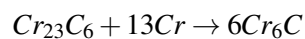
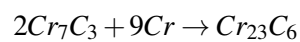
The $M_{23}C_6$ carbides are formed during heat treatment of carbides with a lower M/C ratio or from solid solution close to boundaries [32]. Fine $M_{23}C_6$ carbides act as obstacles to gliding of mobile dislocations, which result in long-term creep strength [33].

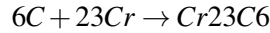
Although $M_{23}C_6$ can precipitate as primary carbide during solidification, it is most commonly found in secondary carbides along grain boundaries.

M_7C_3 is a metastable pseudo-eutectic carbide that typically forms at lower carbon-chromium ratios and effectively transforms into secondary $M_{23}C_6$ upon heat treatment.

In addition to being a carbide former, chromium provides solid solution strengthening and corrosion/oxidation resistance to the cobalt-based matrix.

The Cr_7C_3 carbide is unstable at high temperatures and transforms to $M_{23}C_6$ upon heat treatment. Under further temperature and time, $Cr_{23}C_6$ partially transforms to Cr_6C [34].





The manufacturing process dictates the microstructure of Stellite alloys, with powder metallurgy and additive manufacturing surpass conventional casting and welding. Traditional casting involves slow cooling rates that produce coarse, dendritic microstructures characterized by elemental segregation and a continuous, interdendritic network of carbides.

Welding Stellite alloys onto a substrate creates as-cast microstructure and a fusion zone, where the diffusion of elements alters alloy composition with detrimental phase transformations such as brittle intermetallic compounds [35].

In contrast, thermal spray processes and powder metallurgy (HIPing) produce microstructure that largely retain the originating powder's original microstructure, with thermal spray producing a layered carbide-free microstructure incorporating splats, oxides, & porosity, while HIPing yields a dense, porosity-free and highly homogeneous microstructure with small spherical carbides which impede crack propagation, improving fatigue resistance.

The absence of solidification from a liquid phase prevents element segregation associated with as-cast and as-welded microstructures. [35]

The difficulty with processing make Stellite alloys ideal for powder processing using net shaping techniques.

[7]

Further processing via re-HIPing can induce carbide precipitation, carbide coarsening and additional solid-solution strengthening of the matrix, improving wear performance. Temperatures above 1000C are typically required to ensure homogenisation of the microstructure and reduction in porosity [36].

Recently developed additive manufacturing techniques such as Selective Laser Melting (SLM) and Powder Bed Fusion (PBF) leverage rapid solidification to create fine-grained columnar microstructure.

Ashworth et al [7] found that high carbon Stellite alloys benefitted from higher HIPing temperatures (1200 C) while low carbon Stellite alloys reached optimum properties at a HIPing temperature of 1120 C.

Beyond the process, alloy composition is crucial; high-carbon Stellite alloys exhibit superior wear resistance due to a much larger volume fraction of hard carbides, while the substitution of tungsten with molybdenum can further enhance erosion-corrosion resistance by

modifying the carbide types and strengthening the matrix [7586, 7788, 7992, 3927, 3928, 4080, 4081, 4082].

Yu et al [20] found that HIPed stellite 6 had lower fatigue performance to HIPed stellite 20.

Rehan et al [37]

Wong Kian et al [35] found that HIPed versions of Stellite 1, 6 and 12 consistently showed superior resistance to as-weld overlays in erosion–corrosion tests using a rotating slurry pot configuration.

Stellite 4 [25] Stellite 20 [38] Stellite 6 [20]

	Co	Cr	W	C	Mo	Fe	Ni	Mn	Si
Cast Stellite 4	Bal.	31.7	13.5	0.90	0.20	1.65	0.65	0.56	0.72
HIPed Stellite 4	Bal.	31.0	14.4	0.67	0.12	2.16	1.82	0.26	1.04
Cast Stellite 20	Bal.	34.50	16.50	2.39	0.50	1.50	1.00	0.60	0.78
HIPed Stellite 20	Bal.	31.85	16.30	2.35	0.27	2.50	2.28	0.26	1.00
Cast Stellite 6 alloy	Bal.	27.10	4.95	0.95	0.30	1.10	0.60	0.90	1.24
HIPed Stellite 6 alloy	Bal.	29.50	4.60	1.09	0.22	2.09	2.45	0.27	1.32

As well as the corrosion behaviour being of interest, Malayoglu and Neville [16] conducted a comparative study on the erosion-corrosion performance of both HIPed and investment cast Stellite 6® in 3.5% NaCl solution as a function of temperature and the level of erosive particle loading. They found that in all cases, the HIPed Stellite 6® exhibited the higher erosioncorrosion resistance, which they attributed to the fact that the carbides are not interconnected in the HIPed material whereas eutectic and dendritic carbides in the cast structure form a network of interconnected material. Furthermore, the mean free path between carbides is much smaller in the HIPed material and as such the material responded homogeneously to 4 erosion-corrosion. Another study comparing the erosion-corrosion behaviour of a range of HIPed and weld-deposited Stellite alloys in a nitric acid environment demonstrated that the HIPed alloys generally exhibited a lower mass loss which was again attributed to the finer microstructure [17]. A similar conclusion was also reached by Neville and Malayoglu [18] who attributed the superior corrosion resistance of HIPed Stellite 6 to its microstructure with equiaxed carbides and an absence of areas of chromium-depleted matrix material, due to reduced segregation.

Corrosion performance studies have demonstrated the superiority of HIPed materials.

Malayoglu and Neville evaluated HIPed versus as-cast Stellite 6 in 3.5% NaCl solution under varying temperature and erosive particle loading conditions, with their findings of su-

perior erosion-corrosion resistance in HIPed materials at temperatures up to 90C attributed to homogeneous material response.

Additional investigations in nitric acid environments confirmed reduced mass loss in HIPed alloys [17], with enhanced corrosion resistance attributed to equiaxed carbides and absence of chromium-depleted matrix regions due to reduced segregation [18].

Pitting corrosion

Chromium-rich carbides (M_3C_2 , M_7C_3 , $M_{23}C_6$) and refractory-element-rich carbides (M_6C and MC).

The susceptibility of passivating metals to localized corrosion is dependent on the passive film's physical and chemical structure and ability to resist breakdown and to repassivate once corrosion has initiated.

Malayoglu and Neville [39] find that Stellite 6 shows a multilayer passive film, where the outer surface consists primarily of $Cr(OH)_3$ / Cr_2O_3 and WO_2 , and the inner layer consists of $Cr(OH)_3$ / Cr_2O_3 , metallic Cr & W, and WO_3 , with no evidence of Cl⁻ ion content, unlike that reported for stainless steels.

Wong-Kian et al. [16] showed that under erosion-corrosion conditions HIPed Stellite alloys 1, 6, and 21 had lower mass loss than the welded specimens of the same Stellites. They related their finding to the finer and homogeneous microstructure, which was obtained after HIPing. They also showed that wear resistance of the cobalt-based alloys is promoted by the harder complex carbides of chromium and tungsten, while corrosion resistance is enhanced by the presence of cobalt in the matrix.

1.2 Comparison to Literature

General Microstructure of Cast Alloys

Stellite 4: Features a hypoeutectic microstructure consisting of Co-rich dendrites, a Cr-rich eutectic phase, and W-rich carbides. Stellite 6: Also has a hypoeutectic microstructure with Co-rich dendrites set in a lamellar eutectic of Cr-rich and W-rich carbides. The relatively large carbides suggest a slow cooling rate during casting. Stellite 20: Possesses a hypereutectic microstructure, characterized by large, primary blocky (idiomorphic) Cr-rich carbides surrounded by a dendritic CoCrW solid solution and eutectic phases.

The remarkable ability of Stellite alloys to withstand these specific challenges stems from key metallurgical features. Their corrosion resistance is primarily attributed to a high chromium content, typically 20-30 wt.%, which promotes the formation of a highly stable, tenacious, and

self-healing chromium-rich passive oxide film on the material's surface; this film acts as a barrier isolating the underlying alloy from the corrosive environment. Alloying elements such as molybdenum and tungsten can further enhance this passivity, particularly improving resistance to localized corrosion phenomena like pitting and crevice corrosion in aggressive media. Concurrently, their outstanding cavitation resistance is largely derived from the unique behavior of the cobalt-rich matrix, which can undergo a stress-induced crystallographic transformation from a face-centered cubic (fcc) to a hexagonal close-packed (hcp) structure. This transformation, often facilitated by mechanical twinning, effectively absorbs the intense, localized impact energy from collapsing cavitation bubbles and leads to significant work hardening, thereby impeding material detachment and erosion.

Antony suggests that the cavitation-erosion resistance of Stellites derives from the matrix phase and is enhanced by the strain-induced fcc \rightarrow hcp allotropic transformation [40].

The cavitation erosion of stellites has been investigated in experimental studies [Wang2023, Szala2022741, Mitelea2022967, Liu2022, Sun2021, Szala2021, Zhang2021, Mutascu2019776, Kovalenko2019175, E201890, Ciubotariu2016154, Singh201487, Hattori2014257, Depczynski20131045, Singh2012498, Romo201216, Hattori20091954, Ding201797, Guo2016123, Ciubotariu201698], along with investigations into cobalt-based alloys [Lavigne2022, Hou2020, Liu2019, Zhang20191060, E2019246, Romero2019581, Romero2019518, Lei20119, Qin2011209, Ding200866, Feng2006558].

Stellites achieve oxidation resistance through the formation of a passivating external Cr₂O₃ scale, due to the high proportion of Cr in their chemical composition [41].

as seen by Zhang et al in Green Death solution [42].

However, Cr-based carbides may be preferentially oxidized below the external Cr₂O₃ scale, particularly at the boundary of carbides which are depleted of Cr [42], where preferential attack of carbides proceed until they have been consumed [41].

Mohamed et al find that Stellite exposed to cyclic potentiodynamic polarization in 3% NaCl solution results in slight depletion of Co, accompanies with corresponding enrichment in Cr and W [43].

Mohamed

Lemaire et al [44] investigated the behavior of Stellite 6 in pressurized high temperature water and proposed an oxidative wear mechanism where wear proceeds by repeated detachment of the surface oxide spontaneously forming on the stellite surface.

Di Martino et al [45] also found that the protective chromium-rich film are abraded easily, leading to further corrosion.

In such lower-temperature regimes, the passive films formed are typically very thin (in the nanometer range, rather than the micrometer scale observed at high temperatures)

It is also known for passive alloys that there is generally an inverse relationship between the

thickness of the film and its protective property. This was seen in work by Malayoglu et al.³ where the breakdown potential in anodic polarization tests was shown to be reduced aligned with a thinning of the passive film detected by XPS on HIPed Stellite 6 in 3.5% NaCl [46].

Molybdenum and tungsten have favorable effects on the selective oxidation of chromium until chromium has been depleted, at which point molybdenum and tungsten result in increased oxidation due to development of less protective phases [41].

Chapter 2

Materials and Experimental Test Procedure

The cast Stellite 1 alloys were produced via sand castings. Spherical gas-atomized Stellite 1 powders were used to produce HIPed samples through consolidation in a HIPing vessel at a temperature of 1200C and 100 MPa for 4 hours, as reported in previous work by Ahmed et al [47]. Sieve analysis of the gas-atomized powders indicate that powder particles were in the size range of 45 to 180 um [47], with SEM analysis conducted to measure particle size via image analysis.

	+250	+180	+125	+45	-45
HIPed Stellite 1	0.10	2.40	47.90	49.50	0.10

The microstructure of the alloys were observed via scanning electron microscopy (SEM) using a back-scattered electron imaging detector (BSE), with elemental compositions of the observed phases determined via energy dispersive X-ray spectroscopy (EDS). Image analysis of BSE images was conducted to ascertain area fractions of individual phases.

Microstructure phase analysis was performed with a Bruker Discover D8 <> X-ray diffractometer (XRD) with Cu K_α radiation ($\lambda = 1.5406$) in Bragg-Brentano $\theta : 2\theta$ configuration across the diffraction angle range 20deg <> to 120deg <> with a step size of 0.00deg <>.

The volume fraction of ϵ -Co is calculated via the relative intensity of the $(200)_\gamma$ and $(10\bar{1}1)_{hcp}$ peaks, as proposed by Sage and Guillaud [48].

$$hcp(vol\%) = \frac{I(10\bar{1}1)_\epsilon}{I(10\bar{1}1)_\epsilon + 1.5I(200)_\gamma} \quad (2.1)$$

The Vickers microhardness was measured using a Wilson hardness tester under loads of BLAH. Thirty measurements under each load were conducted on each sample.

2.1 Experimental determination of SFE

To experimentally determine the SFE, the XRD method proposed by Reed and Schramm was employed [49]:

$$SFE = \frac{K_{111}\omega_0 G_{111}a_0}{\pi\sqrt{3}} \frac{\langle \epsilon_{50}^2 \rangle_{111}}{\alpha} A^{-0.37} \quad (2.2)$$

where:

$$K_{111}\omega_0 = 6.6G_{111} = \frac{1}{3} \frac{1}{C_{44} + C_{11} - C_{12}} A = \frac{1C_{44}}{C_{11} - C_{12}} \quad (2.3)$$

ployed [49]:

SFE = stacking fault energy $\frac{mJ}{m^2}$ $K_{111}\omega_0 = 6.6$, as obtained by A is the Zener elastic anisotropy C_{ij} are elastic stiffness coefficients G_{111} is the shear modulus of the (111)-plane, in which stacking faults are formed a_0 is the lattice constant of the fcc-metal matrix $\langle \epsilon_{111}^2 \rangle_{50}$ is the root mean square microstrain in the <111> direction averaged over the distance of 50 α is stacking fault probability

1. Elastic constant

Microhardness measurements were taken on the surfaces of the as-cast and HIPed samples. The Wilson Tukon 1102 hardness tester was used for Vickers microhardness testing with a load of 300 grams ($HV_{0.3}$) for 10s, and averaged by using ten individual indentations. The specimen surface was prepared in the same fashion as for microstructural analysis.

Previous work

The indentation fracture toughness was made with hardness equipment (AVK-A, AKASHI) at a load of 49 N for 10 s, and the value was obtained from five measurements on the cross section. The fracture toughness was evaluated based to the Evans-Wilshaw equation [21, 22].

$$K_{IC} = 0.079 \left(\frac{P}{a^{\frac{3}{2}}} \right) \log \left(\frac{4.5a}{c} \right) \quad (2.4)$$

where P is indenter load [mN], $2c$ is the crack length [μm], and $2a$ is the length of indentation diagonal [μm]

2.2 Electrochemical measurement

A Corrtest CS310 potentiostat was used for electrochemical experiments in a conventional three electrode cell, with the sample as working electrode with exposed area 2cm², a saturated calomel electrode (SCE) as reference electrode, graphite plate as counterelectrode, and naturally aerated 3.5% NaCl solution at room temperature as electrolyte.

After attaching wires to the back of samples with copper tape, epoxy resin was used to seal the sample, ensuring only one surface was exposed. This surface was then ground and polished with 220, 600, & 1000 grit silicon carbide sandpaper, followed by 15um, 6um, 1um, and 0.25um diamond paste. The specimens were rinsed with distilled water, followed by sonication in acetone for 5 minutes, and air-dried for 5 minutes. All samples were freshly prepared before commencement of electrochemical tests.

For all testing, the OCP was monitored for 1 h to ensure steady state conditions, before the electrical impedance spectroscopy (EIS), LPR, and cyclic voltametry (CV) experiments, in addition to a 24 hour exposure period to measure the change of OCP over time.

The EIS spectra was measured across a frequency range of 10^5 Hz to 10^1 Hz and an excitation voltage of 10mV, with 20 evenly spaced frequencies per decade. Duplicate spectra and additional EIS tests conducted at an excitation voltage of 20 mV were measured to verify the validity of the test data EIS should be independent of the excitation voltage. The obtained spectrum was analyzed with the help of Nyquist and Bode plots and equivalent circuit fitting using Corrtest ZView software.

2.3 Experimental electrochemical - polarize electrode to -1.5 to remove oxides

Passivation and corrosion behaviours of cobalt and cobalt–chromium–molybdenum alloy Author links open overlay panelM. Metikoš-Huković , R. Babić <https://www.sciencedirect.com/science/article/pii/S0010938X07000819>

2.4 Description of constant phase element

2.5 Other stuff

A magnetostrictive vibratory apparatus, operating in general accordance with ASTM Standard G32, was utilized. The system functioned at an ultrasonic frequency of 20 kHz, with a peak-to-peak displacement amplitude of the horn tip maintained at 96 μ m. The horn, fabricated from a cavitation-resistant titanium alloy, featured a flat tip of 16 mm diameter. Experiments were conducted using a stationary specimen configuration, with the specimen positioned 0.5 mm below the vibrating horn tip, this distance being precisely set using a dial gauge.

The aqueous oxidation of Stellite 6 alloy was investigated in a 1979 study using X-ray Photoelectron Spectroscopy (XPS) [50]. Specimens were exposed to pH 10 water at 285°C. To understand the oxidation behavior, the study measured dissolved oxygen concentration against exposure duration.

The high-temperature corrosion resistance of stellite coatings is attributable to the formation of cobalt & chromium surface [51].

Heathcock et al found that carbides are selectively eroded, with the carbide-matrix interface acting as initiating erosion site [52].

2. Paragraph 5: Research and Development for Enhanced Corrosion and Cavitation Performance IGNORE

3. Paragraph: Cavitation Erosion Resistance

The primary result of an erosion test is the cumulative mass loss versus time, which is then converted to volumetric loss and mean depth of erosion (MDE) versus time for the purposes of comparison between materials of different densities. The calculation of the mean depth of erosion for this test method should be performed in conformity with ASTM G-32.

4. General Background %cite:@Franc2004265, @Romo201216, @Kumar2024, @Kim200685, @Gao2024, @20221xix, @Usta2023, @Cheng2023, @Zheng2022

Cavitation erosion presents a significant challenge in materials degradation in various industrial sectors, including hydroelectric power, marine propulsion, and nuclear systems, stemming from a complex interaction between fluid dynamics and material response [53, 54]. Hydrodynamically, the phenomenon initiates with the formation and subsequent violent collapse of vapor bubbles within a liquid, triggered by local pressures dropping to the saturated vapor pressure. These implosions generate intense, localized shockwaves and high-speed microjets that repeatedly impact adjacent solid surfaces [55]. From a materials perspective, these impacts induce high stresses (100-1000 MPa) and high strain rates, surpassing material thresholds and leading to damage accumulation via plastic deformation, work hardening, fatigue crack initiation and propagation, and eventual material detachment. Mitigating this requires materials capable of effectively absorbing or resisting this dynamic loading, often under demanding conditions that may also include corrosion.

% Martensitic transformation Crucially, the cobalt matrix often possesses a low stacking fault energy, facilitating a strain-induced martensitic transformation from a metastable face-centered cubic γ phase to a hexagonal close-packed ϵ phase under the intense loading of cavitation. This transformation is a primary mechanism for dissipating impact energy and enhancing work hardening, contributing significantly to Stellite's characteristic cavitation resistance [56, 57].

HIPing is a thermo-mechanical material processing technique which involves the simultaneous application of pressure (up to 200 MPa) and temperature (2000 C), which results in casting densification, porosity closure, and metallurgical bonding. [38]

While commonly applied via casting or weld overlays, processing routes like Hot Isostatic Pressing (HIP) offer potential advantages such as microstructure refinement [58] finer microstructures and enhanced fatigue resistance [37, 38].

HIPing of surface coatings results in microstructure refinement, which can yield improved fatigue and fracture resistance.

HIPing leads to carbide refinement, which can yield improved impact toughness [20], and reduce carbide brittleness [38].

Furthermore, HIP facilitates the consolidation of novel 'blended' alloys created from mixed elemental or pre-alloyed powders, providing a pathway to potentially tailor compositions or microstructures for optimized performance. However, despite the prevalence of Stellite alloys and the known influence of processing on microstructure and properties, the specific cavitation erosion behavior of HIP-consolidated Stellites, particularly these blended formulations, remains underexplored in academic literature. Given that erosion mechanisms in Stellites often involve interactions at the carbide-matrix interface [59], understanding how HIP processing and compositional blending affect these interfaces and the matrix's transformative capacity under cavitation, especially when potentially coupled with corrosion, constitutes a critical knowledge gap addressed by this research.

% Need to describe Stellite 1

2.6 Stellite 1

Stellite 1 is a high-carbon and high-tungsten alloy, making it suitable for demanding applications that require hardness & toughness to combat sliding & abrasive wear [15]

2.7 Stellites

2.8 Objectives and Scope of the Research Work

2.9 Thesis Outline

2.10 Literature Survey

2.11 Cavitation Tests

2.12 Charpy impact energy

	Macrohardness	Microhardness	Charpy Impact Energy
	HV, 294N	HV 2.94N	J
Cast Stellite 20	653.4 pm 18.7	759 pm 98	1.36 pm 0
HIPed Stellite 20	675 pm 17.2	704 pm 15	

Chapter 3

Results and Analysis

3.1 Microstructure and Phase Analysis

Cast Stellite 1 has a hypereutectic structure consisting of M₇C₃ primary carbides, M₆C eutectic carbides, and matrix. HIPed Stellite 1 show the same phases but with much finer structure, with fine carbides uniformly distributed in the matrix.

The different variants of the S1 alloy show a similar content of carbides of type M₇C₃ with 22–24 vol.-%. However, the M₆C content of the HIP variant at 15.8 vol.-% is almost twice as high as that of the cast or welded variant. Accordingly, the total carbide content of the S1 alloys investigated varies between 29.3 and 37.5 vol.-%.

3.2 Microstructure and Phase Analysis

The microstructures of the gas atomised powder particles, cast and HIPed alloys are shown in Fig. 2.

The possible phases in the powders were identified via XRD as -Co (F.C.C.), Cr, Cr₂₃C₆, Co₆W₆C, Co₃W, and Co₇W₆. Fig. 2b shows the hypoeutectic microstructure of the cast alloy, which consists of Co-rich dendrites (dark region), Cr-rich eutectic phase (grey phase), and W-rich carbide (bright phase).

Table II presents the image analysis results of the area fractions of various phases in the cast and HIPed structures.

The XRD analysis revealed that -Co was the primary phase in the Co-rich solid solution, whilst tungsten was also present in the solid solution, which strengthened it by forming the inter-metallic compounds Co₃W and Co₇W₆.

The Cr-rich eutectic phase was unlikely to be pure Cr₂₃C₆ carbide as identified via the XRD analysis, because the relatively lower carbon content (0.9wt.%) of the alloy could not lead to such high area fraction (27.7%) of carbides.

This phase could be a mixture of Cr₂₃C₆ carbides and CoCrW solid solution, as the EDS analysis showed that it consisted of small proportions of Co and W, besides Cr and C. The bright phase was identified as W-rich carbide, Co₆W₆C. The microstructure of the HIPed alloy (Fig. 2c) consisted of three types of phases, which were uniformly distributed in the matrix (dark region),

with an area fraction of 65.8%). The EDS analysis revealed that the light grey phase contained around 35% Co, 28% Cr, and 37% W (in wt.%), indicating that this phase was also CoCrW solid solution, which differed from the matrix phase in terms of its tungsten content. The dark grey phase was Cr-rich carbide with an approximate composition of $(\text{Co}_{0.22}\text{Cr}_{0.70}\text{W}_{0.08})_{23}\text{C}_6$. The bright phase was identified as W-rich carbide. The XRD analysis indicated that the possible phases in the HIPed alloy were γ -Co, Cr_7C_3 , Cr_{23}C_6 , $\text{Co}_6\text{W}_6\text{C}$, Co_3W , and Co_7W_6 . Most of these phases were inherited from the powders, except for the Cr_7C_3 , indicating that it was formed during the HIPing process.

In comparison to the cast alloy, the microstructure of the HIPed alloy was not only finer, but also had discrete carbides, instead of the interconnected three-dimensional eutectic net observed in the cast structure.

The difference in the microstructure can have a significant influence on the tribo-mechanical properties. As discussed later, the impact toughness and fatigue resistance, which involved failure mechanisms that were dependent upon crack propagation, benefited from the absence of a three-dimensional eutectic net in the HIPed alloy. However, there was a trade-off between these improvements, and the wear resistance of the HIPed alloy, as the difference in carbide morphology caused changes in the wear mechanisms.

Figures 2 and 3 provide the SEM and XRD comparison of the cast and HIPed alloys. Figure 2 a shows the SEM of the dendritic microstructure on the spherical surface of the gas-atomized powder. Figure 2 b and 2 c show the hypoeutectic microstructure of the cast alloy, which consists of Cr-rich carbides dark phase, W-rich carbides bright phase, and the Co-rich dendritic matrix gray region. Figure 2 d shows the SEM observation of the HIPed alloy, with finer carbides dark phase uniformly distributed in a Co-rich matrix gray region. The image analysis results of the area fractions of various phases are presented in Table 2. Previously reported 20 image analysis results for Stellite 20 alloys are also presented in this table to aid the discussion.

The cast CoCr28W alloy had a hypoeutectic microstructure Figs. 2 b and 2 c, which consists of Co-rich dendrites gray region, set in lamellar eutectic Cr-rich dark phase and W-rich bright phase carbides. The Cr-rich eutectic carbide had a composition of $\text{Cr}_{0.71}\text{Co}_{0.25}\text{W}_{0.03}\text{Fe}_{0.005}\text{C}_7$, as approximated by the EDS analysis. The XRD analysis Fig. 3 c revealed that the carbides were Cr_7C_3 and $\text{Co}_6\text{W}_6\text{C}$, while γ -Co fcc was the primary phase in the solid solution, together with the intermetallic compounds, Co_3W and Co_7W_6 .

This dendritic microstructure is typical of the cast CoCr28W alloy in which the carbide and grain size can be controlled by the rate of cooling. Within the family of cast cobalt-based alloys, the relatively large carbide size seen in the cast microstructure indicated slow freezing during the casting process. The microstructure of cast Stellite 6 alloys was a topic of research for a number of investigations and further details of the influence of the cooling rate on the grain size

of cast cobalt-based alloys can be appreciated elsewhere 13 . The scope of the discussion here is therefore its microstructural comparison with the HIPed counterpart in terms of understanding the structure-property relationships during tribomechanical performance. The HIPed alloy had a much finer microstructure Fig. 2 d with Cr-rich carbides dark phase uniformly distributed in the matrix.

The typical carbide size was 1 – 3 μm , which was much finer than the cast counterpart. There was no bright W-rich phase observed in the HIPed microstructure, which could be attributed to the fast solidification in the powder manufacturing process, restricting the segregation of W-rich zones. Subsequently during HIPing of the powder, tungsten remained evenly distributed throughout the alloy because its large atomic radius hinders diffusion. This evolution of the HIPed microstructure was therefore fundamentally different from the dendritic microstructure of the cast alloy, which was caused by the rejection of elemental species in the melt during the crystal growth of Co-rich dendrites. Hence above the liquidus line of this complex Co alloy, elemental species were free to arrange themselves depending on the thermal kinetics of the mold without any dependency on diffusion, and hence a truly three-dimensional network of carbides was formed. Contrary to this, in the case of HIPed microstructure, the primary dendrites formed on the alloy powder Fig. 2 a , and the carbides in the powder particles Fig. 3 a promoted carbide growth due to the diffusion of carbon and other elemental species within and across the individual powder particle boundaries.

As this diffusion process is time, temperature, and pressure dependent during HIPing, and the HIPing temperature 1200° C in this investigation was lower than the melting point of the powder, carbide growth was sluggish when compared with casting. Hence the size of individual carbide particles was much smaller than the cast counterpart.

Although not reported in Sec. 3, authors also found that re-HIPing the HIPed alloy under similar conditions as were reported earlier in Sec. 2.1 did not substantially increase the average carbide size, indicating that carbide growth was more dependent on temperature than time during the HIPing process. The XRD analysis Fig. 3 b revealed that the possible phases in the HIPed alloy were Cr_7C_3 , -Co, Co_3W , and Co_7W_6 , which were similar to those in the cast alloy, except the absence of $\text{Co}_6\text{W}_6\text{C}$. The intermetallic compound, Co_7W_6 , was not identified in the atomized powder, indicating that it was formed during the HIPing process. The pure Cr phase in the powder, which formed due to the rapid solidification, was not identified in the HIPed alloy, indicating that it either combined with the cobalt matrix, or formed carbides. The image analysis Table 2 showed that the cast alloy had an approximate total carbide fraction of 15.5%, which was slightly less than that of the HIPed alloy 17.9%.

These values indicated on average a 63% reduction in the carbide content when compared with the Stellite 20 alloy, which can be attributed to the lower carbon and tungsten content in the

Stellite 6 alloys. These differences in the microstructure, carbide content, and morphology had a significant influence on the tribomechanical performance, as discussed in the following sections.

4.1 Microstructure. The microstructure of cobalt-based Stellite alloys has been the topic of research for almost a century and a number of investigations have discussed their microstructure on the basis of alloy composition and processing route 4,5,10–17 . However, comparative analysis of the microstructure of these alloys is scarce in the published literature. The aim of the discussion here is therefore to highlight the differences in the microstructure of the two alloys, with a view to underpin the understanding of structure–property and tribo-mechanical behavior. The cast alloy had a hypereutectic microstructure, which was typical of cobalt-based alloys of this composition. The primary idiomorphic carbide was Cr-rich M_7C_3 , with a composition of $Cr_{0.75}Co_{0.20}W_{0.05}C_3$, as approximated by the EDS analysis. These are rod like carbides, a section of which can be seen as the dark blocky carbide in Fig. 2 b . It was surrounded by the dendritic CoCrW solid solution grey region . The final phases to solidify were the lamellar eutectic phases containing both the Cr-rich dark and W-rich light carbides. The three-phase area shown in Fig. 2 b indicates the simultaneous occurrence of both primary carbides and CoCrW dendrites in the microstructure. The XRD analysis Fig. 3 b revealed that the carbides were Cr_7C_3 , $Cr_{23}C_6$, and Co_6W_6C , while the primary phase in the solid solution was γ -cobalt fcc , together with the intermetallic compounds, Co_3W and Co_7W_6 . Hence, in the cast alloy, there were three kinds of carbides, i.e., the relatively large blocky Cr-rich carbides, the interconnected three-dimensional W-rich eutectic carbides, and the relatively smaller Cr-rich eutectic carbides, which coexisted in the microstructure. The HIPed alloy had a finer microstructure Fig. 2 c with Cr-rich dark and W-rich light carbides uniformly distributed in the matrix. These carbides were typically 2 μm in size and much finer than the large blocky carbides observed in the cast alloy. Despite different microstructure, the possible phases identified in the HIPed alloy were similar to those in the cast alloy Fig. 3 . These phases seemed to be inherited from the atomized powders, except for the replacement of Co_3W_3C by Co_6W_6C . The pure chromium phase identified in the powder, which formed due to the rapid solidification from the molten state during the atomization process, was not identified in the HIPed alloy. This indicated that it either was combined with cobalt, or formed carbides, and no longer existed as a pure phase after the HIPing process. The total volume fraction of carbides Table 2 was nearly 50% in the HIPed alloy, which were uniformly distributed in the metal matrix Fig. 2 c . The differences in the carbide morphology of both alloys can have a significant influence on their tribomechanical properties. In terms of the structure–property relationships, as discussed in later sections, the failure mechanisms, which were very much dependent upon crack propagation, e.g., impact and fatigue strength, therefore benefitted significantly from the absence of a three-dimensional eutectic net in the HIPed alloy. However, there was a tradeoff between the improved impact strength and relatively lower wear resistance due to smaller carbides in the HIPed alloy,

because of the changes in the wear mechanisms during the abrasive and sliding wear of the two alloys. The image analysis Table 2 indicated that despite similar volume fractions of Cr-rich carbides in both alloys, the approximate W-rich carbides content in the HIPed alloy 24.7% was more than that in the cast alloy 18.1% . In view of the higher carbide content, one might expect superior abrasive and sliding wear performance of the HIPed alloy. However, as discussed later, the changes in the wear mechanisms due to the relatively smaller size of carbides observed in the HIPed microstructure, did not provide significant abrasive wear improvement over the cast counterpart.

3.3 Electrochemical corrosion tests

1. Open circuit potential measurement

These two below do a great job of

Open circuit potential measurements observe the unaltered corroding potential in the absence of any applied external voltage/current, with passivating alloys expected to reach a steady state potential [60, 61], in order to establish an equilibrium condition from which to perform further electrochemical tests. As seen in Fig <>, the HIPed Stellite 1 initially shows an OCP of <> mV (SCE) which increases to more noble potentials, reaching <> mV (SCE) after 24 hours, while the cast Stellite 1 specimen shows an initial OCP of <> mV (SCE) which increases to <> mV (SCE) after the same exposure duration.

Although both HIPed and cast specimens are observed to have OCPs drift towards less negative potentials, which is indicative of the formation of a passive oxide film, the HIPed alloy consistently shows higher OCP values, suggesting a greater thermodynamic inclination for oxide film formation and better corrosion protection in 3.5% NaCl solution.

2. Polarization Tests

3.4 Strain hardening

Cavitation bubble collapses cause significant plastic deformation and strain-induced work hardening in the near-surface of ductile materials, characterized by the thickness of the hardened layers and the shape of the strain profile below the surface [berchicheCavitationErosionModel2002].

In cobalt-based alloys, work hardening is primarily attributable to a strain-induced martensitic phase transformation from the metastable γ -Co phase to the harder ϵ -Co phase. Woodford's investigations on the γ/ϵ transformation on the surface of cobalt-base alloys during cavitation erosion, the transformed layer was found to extend to a depth of 25 to 50 through XRD analysis

[19], with the percentage of transformation remaining constant with cavitation erosion.

This analysis was first proposed by Karimi & Leo in 1987 [62] and adapted by Berniche et al in 2002 [berchicheCavitationErosionModela], and Franc [63] in 2009.

The strain profile within the material can usually be modeled by the following power law:

$$\varepsilon(x) = \varepsilon_s \left(1 - \frac{x}{L}\right)^\theta \tag{3.1}$$

where $\varepsilon(x)$ is the strain at depth x from the eroded surface, ε_s is the failure rupture strain on the eroded surface, L is the thickness of the hardened layer, θ is the shape factor of the power law. The parameters L and θ are determined from the microhardness measurements on cross sections of the cavitation affected region.

The strain hardening effect after erosion tests was calculated from the following formula:

$$\Delta HV = \frac{HV_x - HV_0}{HV_0} \cdot 100\% \tag{3.2}$$

where HV_x is the hardness at a distance below the cavitation crater, while HV_0 is the initial hardness.

1. Data for strain hardening IGNORE
Table 3.1: Microhardness HV_{0.01} of Al0.1CoCrFeNi HEA
[nairExceptionallyHighCavitation2018a]

x	y
15.025380710659899	339.3103448275862
29.949238578680202	277.2413793103448
44.87309644670051	212.0689655172414
59.974619289340104	230.34482758620692
74.89847715736042	203.10344827586206
89.82233502538071	203.44827586206895
104.74619289340102	195.86206896551724
120.0253807106599	195.86206896551724
135.12690355329948	187.58620689655174
150.2284263959391	155.86206896551724
164.9746192893401	153.10344827586206

Table 3.2: Microhardness $HV_{0.01}$ of 316LSS [**nairExceptionallyHighCavitation2018a**]

x	y
14.847715736040609	288.62068965517244
29.77157360406091	251.72413793103448
45.0507614213198	240
59.974619289340104	219.31034482758622
74.89847715736042	227.24137931034483
89.82233502538071	228.9655172413793
104.9238578680203	221.72413793103448
120.0253807106599	218.27586206896552
135.48223350253807	224.82758620689657
149.87309644670052	225.86206896551727
165.1522842639594	224.48275862068965

Chapter 4

Discussion

4.1 Experimental Test Procedure

4.1.1 Hardness Tests

4.1.2 Cavitation

4.2 Relationships between cavitation erosion resistance and mechanical properties

4.3 Influence of vibratory amplitude

% Insert the whole spiel by that French dude about displacement and pressure (and then ruin it) The pressure of the solution depends on the amplitude of the vibratory tip attached to the ultrasonic device. Under simple assumptions, kinetic energy of cavitation is proportional to the square of the amplitude and maximum hammer pressure is proportional to A.

$$x = A \sin(2\pi ft) \quad (4.1)$$

$$v = \frac{dx}{dt} = 2\pi f A \cos(2\pi ft) \quad (4.2)$$

$$v_{max} = 2\pi f A \quad (4.3)$$

$$v_{mean} = \frac{1}{\pi} \int_0^\pi A \sin(2\pi ft) = 4fA \quad (4.4)$$

$$(4.5)$$

However, several researchers have found that erosion rates are not proportional to the second power of amplitude, but instead a smaller number. Thiruvengadam [64] and Hobbs find that erosion rates are proportional to the 1.8 and 1.5 power of peak-to-peak amplitude. Tomlinson et al find that erosion rate is linearly proportional to peak-to-peak amplitude in copper [3]. Maximum erosion rate is approximately proportional to the 1.5 power of p-p amplitude [4]. The propagation of ultrasonic waves may result in thermal energy absorption or into chemical energy, resulting in reduced power. For the purposes of converting data from studies that do not use an amplitude of 50um, a exponent factor of 1.5 has been applied.

4.4 Correlative empirical methods

Empirical methods are common for addressing complex cavitation erosion, involving lab tests to correlate cavitation erosion resistance with mechanical properties.

1. Karimi and Leo

The Karimi and Leo phenomenological model describes cavitation erosion rate as a function of

Karimi and Leo

2. Noskievic

Noskievic formulated a mathematical relaxation model for the dynamics of the cavitation erosion using a differential equation applied to forced oscillations with damping:

$$\frac{d^2 v}{dt^2} + 2\alpha \frac{dv}{dt} + \beta^2 v = I \quad (4.6)$$

where I is erosion intensity, which can vary linearly with time, $v = \frac{dv}{dt}$ is erosion rate, α is strain hardening or internal friction of material during plastic deformation, and β is coefficient inversely proportional to material strength. The general solution of equation can be written as:

$$v = af_0(\delta, \tau) + bf_1(\delta, \tau) \quad (4.7)$$

$$f_0(\delta, \tau) = \begin{cases} 1 - \exp(-\delta\tau) \left[\frac{\delta}{\omega} \sin(\omega\tau) + \cos(\omega\tau) \right] & \text{if } -1 < \delta < 1; \delta \neq 0 \\ 1 - \frac{1}{\delta_0^2 - 1} \left[\delta_0^2 \exp\left(-\frac{\tau}{\delta_0}\right) - \exp(-\delta_0\tau) \right] & \text{if } \delta > 1 \\ 1 - \cos(\tau) & \text{if } \delta = 0 \\ 1 - (1 + \tau) \exp(-\tau) & \text{if } \delta = 1 \end{cases} \quad (4.8)$$

$$f_1(\delta, \tau) = \begin{cases} 1 - \frac{2\delta}{\tau} [1 - \exp(-\delta\tau) [\cos\omega\tau + \varepsilon \sin\omega\tau]] & \text{if } -1 < \delta < 1; \delta \neq 0 \\ 1 - \frac{1}{\tau} \left(2\delta - \frac{1}{\delta_0(\delta_0^2 - 1)} \left[\exp(-\delta_0\tau) - \delta^4 \exp\left(\frac{-\tau}{\delta_0}\right) \right] \right) & \text{if } \delta > 1 \\ 1 - \frac{\sin(\tau)}{\tau} & \text{if } \delta = 0 \\ 1 - \frac{2[1 - \exp(-\tau)]}{\tau} + \exp(-\tau) & \text{if } \delta = 1 \end{cases} \quad (4.9)$$

$$\delta = \frac{\alpha}{\beta}, \quad \tau = \beta t, \quad \varepsilon = \frac{\delta^2 - 0.5}{\delta \sqrt{1 - \delta^2}}, \quad \omega = \sqrt{1 - \delta^2}, \quad \delta_0 = \delta + \sqrt{\delta^2 - 1} \quad (4.10)$$

3. Hoff and Langbein equation

Hoff and Langbein proposed a simple exponential function for the rate of erosion, representing the normalized erosion rate requiring only the A simple exponential function for the rate of erosion was proposed by Hoff and Langbein,

$$\frac{\dot{e}}{e_{max}} = 1 - e^{-\frac{t_i}{t}}$$

\dot{e} - erosion rate at any time t e_{max} - Maximum of peak erosion rate t_i - incubation period (intercept on time axis extended from linear portion of erosion-time curve) t - exposure time

4. L Sitnik model

$$V = V_o \left[\ln \left(\frac{t}{t_o} + 1 \right) \right]^\beta$$

$$\dot{V} = \frac{\beta V_o}{t + t_o} \left[\ln \left(\frac{t}{t_o} + 1 \right) \right]^{\beta-1}$$

$$V_o > 0 \quad t_o > 0 \quad \beta \geq 1$$

Chapter 5

Conclusions

Part II

Weird hanger-ons

Chapter 6

Erosion particles

<https://www.sciencedirect.com/science/article/pii/S0264127525003065> Experimental investigation of cavitation erosion-induced surface damage and particle shedding from PTFE

Is for PTFE, but the depth of analysis is excellent

Chapter 7

Reasons for why CE is less in seawater

<https://www.sciencedirect.com/science/article/pii/S0043164825000614>

Chapter 8

Residual Stress and why it's important

There is a direct relationship between the cavitation intensity and changes in the residual surface stresses: the higher the level of the cavitation intensity the faster is the build-up of compressive residual stress. However, the maximum value of the cavitation-induced stresses does not depend on the intensity of cavitation. After a sufficiently long attack time the same maximum value is reached, even at points of lowest cavitation intensity. The reduction in compressive residual stress which can be observed after a long cavitation time is due to the plasticity being exhausted and the related formation of microcracks. During the initial phase of the attack, up to the time the limiting stress value is reached, the local variation in cavitation intensity may be very clearly seen in the stress distribution in the surface. Based on the residual stress distribution, it can be ascertained at which point there is a minimum or maximum cavitation intensity and where the removal of the material initially takes place. X-ray residual stress analysis can therefore be valuable for the early detection of cavitation processes.

Chapter 9

Why HIP is better than cast

The microstructure in the Stellite alloys produced by using casting method consisted of the dendrites formed by the Co solid solution and the eutectic carbide phases between these dendrites. The carbides were in the form of continuous films surrounding the grains and had a large size [5], [15], [25], [26], [33]. In the alloys produced by casting, this shape, size, and distribution style of the carbides decreased ductility and fatigue strength of the material [34]. In the present study, it was observed in the material produced by using PIM that the non-interconnected carbides with the block morphology had a homogenous distribution on the grain boundaries throughout the microstructure instead of large size eutectic carbides surrounding the dendrites. Various studies have reported that the carbides exhibited such a distribution in the Stellite alloys produced by using HIP and they had a spherical-like form [5], [15], [25]. The morphology of the carbide precipitates in superalloys has significant effects on the properties of alloys. The fact that carbide precipitates at the grain boundaries in the form of a continuous film sets a ground for the formation of cracks and decreases significantly the impact and rupture properties of the alloy. Since the formation of precipitates that are large and independent from each other (discrete) at the grain boundaries, instead of a continuous film, prevents dramatically the grain boundary sliding, it is useful [23], [35]. Additional heat treatments are needed in Co alloys produced by casting in order to obtain a more homogenous structure by dissolving the large carbide network and thus to improve the mechanical properties [34]. Taking into account these explanations and in contrast to the Stellite alloys produced by casting, it is also expected for the PIM method, which provides the acquiring of materials containing carbides exhibiting finer and more homogenous distribution without needing additional heat treatments, to provide more superior mechanical properties.

Chapter 10

Equiaxed grains - why HIP is better than cast

Numerous previous studies have reported that the materials produced by using PIM consist of equiaxed grains as in this study [18], [19], [20], [21]. The controlling of the grain size is very significant to develop and sustain the physical and mechanical properties among the materials.

In this study, the superior properties such as homogenous microstructure, fine and equiaxed grains easily obtained by using PIM technique without needing any precaution were rather difficult to be obtained by using casting method.

Chapter 11

Describing SEM images (light gray, dark, light)

It can be seen from the SEM images in Fig. 8 that the microstructure included light colored and dark colored phases although no etching process was performed. In the previous studies conducted concerning Stellite alloys, it is reported that the Co matrix in the microstructure was light gray and the carbides rich in Cr were dark gray [3], [5], [15], [26], [29]. It is indicated that W element also forms carbides in Co based superalloys and the carbides formed by W were of a brilliant white color in the microstructure [26]. Based on these explanations, it can be asserted that the dark precipitates homogenously distributed in the microstructure in the SEM images of the samples taken without etching them in this study were the carbides formed by Cr.

Chapter 12

Stellite 1

Chapter 13

Parametric studies on Stellite

Accelerated discovery of composition-carbide-hardness linkage of Stellite alloys assisted by image recognition <https://doi.org/10.1016/j.scriptamat.2023.115539>

Abstract Stellite alloys are widely utilized in the aerospace industry due to their excellent hardness and high wear resistance. Optimal properties are predominantly achieved through engineering desired microstructures in terms of type, size, shape, and spatial distribution of carbides within the Co-Cr matrix through alloying. However, a quantitative linkage among composition, carbide, and hardness (CCH) is still lacking. Herein, we attempt to tailor the essential reinforcement elements, Mo and C, to obtain different Stellite alloys using powder metallurgy (PM). With the help of image recognition technology, microstructures of alloys (including the type and content of carbides, as well as the content of defects.) were quantitatively analyzed. Besides, mathematical algorithms based on Analysis of Variance (ANOVA) and Desirability Functional Analysis (DFA) were developed to establish the models for the quantification of CCH. Specifically, the regression equations provide the quantitative relationship between elements (Mo and C), two primary carbides (M₇C₃ (M=Metal) and M₂₃C₆), and the hardness. We believe this quantitative work assisted by image recognition would be beneficial for the development of Stellite alloys and could shed light on the CCH relationship of other cemented carbides alloys.

Link between Composition/Carbide/Hardness

In general, the chemical composition of Stellite alloys determines the type and content of carbide thus the related mechanical properties. Therefore, the linkage between composition, carbide, and hardness characteristics (CCH) has always been a focus of substantial Stellite alloy studies [3,4,[7], [11], [12], [13], [14]].

Besides, we used the Thermo-Calc software [26] and TCHEA5 thermodynamic database [27] to calculate the phase fraction of each sample at different temperatures as shown in the Fig. S5. The thermodynamic calculation well verified that there is no M₂₃C₆ carbide in the S3 sample. What's more, as shown in the following Table 5, we listed the phase fraction and temperature which are closest to the experimental results according to the CALPHAD results.

References

- [1] R. Ahmed, H. L. de Villiers Lovelock, N. H. Faisal, and S. Davies, "Structure–property relationships in a CoCrMo alloy at micro and nano-scales," *Tribology International*, vol. 80, pp. 98–114, Dec. 1, 2014, ISSN: 0301-679X. DOI: [10.1016/j.triboint.2014.06.015](https://doi.org/10.1016/j.triboint.2014.06.015). Accessed: Jun. 30, 2024. [Online]. Available: <https://www.sciencedirect.com/science/article/pii/S0301679X14002436>.
- [2] J.-C. Shin, J.-M. Doh, J.-K. Yoon, D.-Y. Lee, and J.-S. Kim, "Effect of molybdenum on the microstructure and wear resistance of cobalt-base Stellite hardfacing alloys," *Surface and Coatings Technology*, vol. 166, no. 2, pp. 117–126, Mar. 24, 2003, ISSN: 0257-8972. DOI: [10.1016/S0257-8972\(02\)00853-8](https://doi.org/10.1016/S0257-8972(02)00853-8). Accessed: Jun. 2, 2025. [Online]. Available: <https://www.sciencedirect.com/science/article/pii/S0257897202008538>.
- [3] M. S. Hasan, A. M. Mazid, and R. Clegg, "The Basics of Stellites in Machining Perspective," *International Journal of Engineering Materials and Manufacture*, vol. 1, no. 2, pp. 35–50, Dec. 19, 2016, ISSN: 0128-1852. DOI: [10.26776/ijemm.01.02.2016.01](https://doi.org/10.26776/ijemm.01.02.2016.01). Accessed: May 11, 2025. [Online]. Available: <https://deerhillpublishing.com/index.php/ijemm/article/view/13>.
- [4] U. Malayoglu and A. Neville, "Comparing the performance of HIPed and Cast Stellite 6 alloy in liquid–solid slurries," *Wear*, 14th International Conference on Wear of Materials, vol. 255, no. 1, pp. 181–194, Aug. 1, 2003, ISSN: 0043-1648. DOI: [10.1016/S0043-1648\(03\)00287-4](https://doi.org/10.1016/S0043-1648(03)00287-4). Accessed: Feb. 17, 2025. [Online]. Available: <https://www.sciencedirect.com/science/article/pii/S0043164803002874>.
- [5] D. Raghu and J. B. C. Wu, "Recent Developments In Wear And Corrosion Resistant Alloys For Oil Industry," presented at the Corrosion97, OnePetro, Mar. 9, 1997. Accessed: Jun. 2, 2025. [Online]. Available: <https://dx.doi.org/>.
- [6] M. Alimardani, V. Fallah, A. Khajepour, and E. Toyserkani, "The effect of localized dynamic surface preheating in laser cladding of Stellite 1," *Surface and Coatings Technology*, vol. 204, no. 23, pp. 3911–3919, Aug. 25, 2010, ISSN: 0257-8972. DOI: [10.1016/j.surfcoat.2010.05.009](https://doi.org/10.1016/j.surfcoat.2010.05.009). Accessed: Jun. 2, 2025. [Online]. Available: <https://www.sciencedirect.com/science/article/pii/S0257897210003701>.
- [7] M. Ashworth, M. Jacobs, and S. Davies, "Microstructure and property relationships in HIPed Stellite powders," *Powder Metallurgy*, vol. 42, no. 3, pp. 243–249, Mar. 1, 1999,

- ISSN: 0032-5899. DOI: [10.1179/003258999665585](https://doi.org/10.1179/003258999665585). Accessed: Apr. 3, 2025. [Online]. Available: <https://journals.sagepub.com/action/showAbstract>.
- [8] P. O. Bunch, M. P. Hartmann, and T. A. Bednarowicz, "Corrosion/Galling Resistant Hardfacing Materials for Offshore Production Valves," presented at the Offshore Technology Conference, OnePetro, May 1, 1989. DOI: [10.4043/6070-MS](https://doi.org/10.4043/6070-MS). Accessed: Jun. 2, 2025. [Online]. Available: <https://dx.doi.org/10.4043/6070-MS>.
- [9] V. M. Desai, C. M. Rao, T. H. Kosel, and N. F. Fiore, "Effect of carbide size on the abrasion of cobalt-base powder metallurgy alloys," *Wear*, vol. 94, no. 1, pp. 89–101, Feb. 15, 1984, ISSN: 0043-1648. DOI: [10.1016/0043-1648\(84\)90168-6](https://doi.org/10.1016/0043-1648(84)90168-6). Accessed: Nov. 17, 2024. [Online]. Available: <https://www.sciencedirect.com/science/article/pii/0043164884901686>.
- [10] M. M. Ferozhkhan, K. G. Kumar, and R. Ravibharath, "Metallurgical Study of Stellite 6 Cladding on 309-16L Stainless Steel," *Arabian Journal for Science and Engineering*, vol. 42, no. 5, pp. 2067–2074, May 1, 2017, ISSN: 2191-4281. DOI: [10.1007/s13369-017-2457-7](https://doi.org/10.1007/s13369-017-2457-7). Accessed: Mar. 31, 2025. [Online]. Available: <https://doi.org/10.1007/s13369-017-2457-7>.
- [11] W. Pacquentin, P. Wident, J. Varlet, T. Cailloux, and H. Maskrot, "Temperature influence on the repair of a hardfacing coating using laser metal deposition and assessment of the repair innocuity," *Journal of Advanced Joining Processes*, vol. 11, p. 100 284, Jun. 1, 2025, ISSN: 2666-3309. DOI: [10.1016/j.jajp.2025.100284](https://doi.org/10.1016/j.jajp.2025.100284). Accessed: Mar. 31, 2025. [Online]. Available: <https://www.sciencedirect.com/science/article/pii/S2666330925000056>.
- [12] V. L. Ratia, D. Zhang, M. J. Carrington, J. L. Daure, D. G. McCartney, P. H. Shipway, and D. A. Stewart, "Comparison of the sliding wear behaviour of self-mated HIPed Stellite 3 and Stellite 6 in a simulated PWR water environment," *Wear*, 22nd International Conference on Wear of Materials, vol. 426–427, pp. 1222–1232, Apr. 30, 2019, ISSN: 0043-1648. DOI: [10.1016/j.wear.2019.01.116](https://doi.org/10.1016/j.wear.2019.01.116). Accessed: Jun. 30, 2024. [Online]. Available: <https://www.sciencedirect.com/science/article/pii/S004316481930211X>.
- [13] K. Zhang and L. Battiston, "Friction and wear characterization of some cobalt- and iron-based superalloys in zinc alloy baths," *Wear*, vol. 252, no. 3, pp. 332–344, Feb. 1, 2002, ISSN: 0043-1648. DOI: [10.1016/S0043-1648\(01\)00889-4](https://doi.org/10.1016/S0043-1648(01)00889-4). Accessed: Apr. 1, 2025. [Online]. Available: <https://www.sciencedirect.com/science/article/pii/S0043164801008894>.

- [14] R. Ahmed, H. L. de Villiers Lovelock, and Susan Davies, "Sliding wear of blended cobalt based alloys," *Wear*, vol. 466–467, p. 203 533, Feb. 15, 2021, ISSN: 0043-1648. DOI: [10.1016/j.wear.2020.203533](https://doi.org/10.1016/j.wear.2020.203533). Accessed: Jul. 13, 2024. [Online]. Available: <https://www.sciencedirect.com/science/article/pii/S0043164820309923>.
- [15] P. Crook, "Cobalt-base alloys resist wear, corrosion, and heat," *Cobalt-base alloys resist wear, corrosion, and heat*, vol. 145, no. 4, pp. 27–30, 1994, ISSN: 0882-7958.
- [16] Y. Wu, Y. Liu, H. Chen, Y. Chen, H. Li, and W. Yi, "Microstructure evolution and crack propagation feature in thermal fatigue of laser-deposited Stellite 6 coating for brake discs," *Surface and Coatings Technology*, vol. 358, pp. 98–107, Jan. 25, 2019, ISSN: 0257-8972. DOI: [10.1016/j.surfcoat.2018.11.011](https://doi.org/10.1016/j.surfcoat.2018.11.011). Accessed: May 17, 2025. [Online]. Available: <https://www.sciencedirect.com/science/article/pii/S0257897218312210>.
- [17] R. Lizárraga, F. Pan, L. Bergqvist, E. Holmström, Z. Gercsi, and L. Vitos, "First Principles Theory of the hcp-fcc Phase Transition in Cobalt," *Scientific Reports*, vol. 7, no. 1, p. 3778, Jun. 19, 2017, ISSN: 2045-2322. DOI: [10.1038/s41598-017-03877-5](https://doi.org/10.1038/s41598-017-03877-5). Accessed: May 18, 2025. [Online]. Available: <https://www.nature.com/articles/s41598-017-03877-5>.
- [18] A. Frenk and W. Kurz, "Microstructural effects on the sliding wear resistance of a cobalt-based alloy," *Wear*, vol. 174, no. 1, pp. 81–91, May 1, 1994, ISSN: 0043-1648. DOI: [10.1016/0043-1648\(94\)90089-2](https://doi.org/10.1016/0043-1648(94)90089-2). Accessed: Feb. 18, 2025. [Online]. Available: <https://www.sciencedirect.com/science/article/pii/0043164894900892>.
- [19] D. A. Woodford, "Cavitation-erosion-Induced phase transformations in alloys," *Metallurgical Transactions*, vol. 3, no. 5, pp. 1137–1145, May 1972, ISSN: 0026-086X, 2379-0083. DOI: [10.1007/BF02642445](https://doi.org/10.1007/BF02642445). Accessed: May 18, 2025. [Online]. Available: <https://link.springer.com/10.1007/BF02642445>.
- [20] H. Yu, R. Ahmed, H. d. V. Lovelock, and S. Davies, "Influence of Manufacturing Process and Alloying Element Content on the Tribomechanical Properties of Cobalt-Based Alloys," *Journal of Tribology*, vol. 131, no. 011601, Dec. 4, 2008, ISSN: 0742-4787. DOI: [10.1115/1.2991122](https://doi.org/10.1115/1.2991122). Accessed: May 1, 2025. [Online]. Available: <https://doi.org/10.1115/1.2991122>.
- [21] Y. Ding, R. Liu, X. Zhang, M. Yao, Z. Yao, and J. Yao, "Study of Carbide Precipitation in Two Cobalt-Based Alloys with Distinct Chromium and Tungsten Contents," *Journal of Materials Engineering and Performance*, vol. 30, no. 8, pp. 5962–5973, Aug. 1, 2021, ISSN: 1544-1024. DOI: [10.1007/s11665-021-05786-1](https://doi.org/10.1007/s11665-021-05786-1). Accessed: Jun. 12, 2025. [Online]. Available: <https://doi.org/10.1007/s11665-021-05786-1>.

- [22] M. Morris, "Standard x-ray diffraction powder patterns: Section 21- data for 92 substances," DOI: [10.6028/NBS.MONO.25-21](https://doi.org/10.6028/NBS.MONO.25-21).
- [23] C. Zhang, H. Yin, J. Lv, Y. Du, Z. Tan, and Y. Liu, "Thermodynamic investigation of phase equilibria on the (W,Mo)C-(Co,Ni) cemented carbides," *Calphad*, vol. 67, p. 101664, Dec. 1, 2019, ISSN: 0364-5916. DOI: [10.1016/j.calphad.2019.101664](https://doi.org/10.1016/j.calphad.2019.101664). Accessed: May 18, 2025. [Online]. Available: <https://www.sciencedirect.com/science/article/pii/S0364591619301051>.
- [24] C. Zhang, Y. Peng, P. Zhou, and Y. Du, "Thermodynamic Modeling of the C-Co-Mo and C-Mo-Ni Ternary Systems," *Journal of Phase Equilibria and Diffusion*, vol. 37, no. 4, pp. 423–437, Aug. 1, 2016, ISSN: 1863-7345. DOI: [10.1007/s11669-016-0471-1](https://doi.org/10.1007/s11669-016-0471-1). Accessed: May 18, 2025. [Online]. Available: <https://doi.org/10.1007/s11669-016-0471-1>.
- [25] H. Yu, R. Ahmed, H. d. V. Lovelock, and S. Davies, "Tribo-Mechanical Evaluations of Cobalt-Based (Stellite 4) Alloys Manufactured via HIPing and Casting," 2007.
- [26] M. Zhao, H. Huang, T. Tang, and X. Li, "First-principles study on the preferential sites of Cr in Co_7W_6 ," *Materials Research Express*, vol. 10, no. 3, p. 036502, Mar. 1, 2023, ISSN: 2053-1591. DOI: [10.1088/2053-1591/aca5ef](https://doi.org/10.1088/2053-1591/aca5ef). Accessed: May 18, 2025. [Online]. Available: <https://iopscience.iop.org/article/10.1088/2053-1591/aca5ef>.
- [27] A. S. Kurlov and A. I. Gusev, "Phase equilibria in the W–C system and tungsten carbides," *Russian Chemical Reviews*, vol. 75, no. 7, pp. 617–636, Jul. 31, 2006, ISSN: 0036-021X, 1468-4837. DOI: [10.1070/RC2006v075n07ABEH003606](https://doi.org/10.1070/RC2006v075n07ABEH003606). Accessed: May 11, 2025. [Online]. Available: <https://iopscience.iop.org/article/10.1070/RC2006v075n07ABEH003606>.
- [28] H. Tulhoff, "Carbides," in *Ullmann's Encyclopedia of Industrial Chemistry*, Wiley-VCH, Ed., 1st ed., Wiley, Jun. 15, 2000, ISBN: 978-3-527-30385-4 978-3-527-30673-2. DOI: [10.1002/14356007.a05_061](https://doi.org/10.1002/14356007.a05_061). Accessed: May 11, 2025. [Online]. Available: https://onlinelibrary.wiley.com/doi/10.1002/14356007.a05_061.
- [29] W. H. Jiang, X. D. Yao, H. R. Guan, and Z. Q. Hu, "Secondary M₆C Precipitation in a Cobalt–base Superalloy," *Journal of Materials Science Letters*, vol. 18, no. 4, pp. 303–305, Feb. 1, 1999, ISSN: 1573-4811. DOI: [10.1023/A:1006627122234](https://doi.org/10.1023/A:1006627122234). Accessed: May 12, 2025. [Online]. Available: <https://doi.org/10.1023/A:1006627122234>.
- [30] A. G. Poshtahani, S. Roostaie, and M. Azadi, "Plasma nitriding effect on tribological and corrosion properties of Stellite 6 and 12 PTA weld clad hardfaced on stainless steel 410," *Results in Surfaces and Interfaces*, vol. 11, p. 100108, May 2023, ISSN: 26668459. DOI:

- 10.1016/j.rsurfi.2023.100108. Accessed: Jun. 8, 2025. [Online]. Available: <https://linkinghub.elsevier.com/retrieve/pii/S2666845923000132>.
- [31] Y. Li, Y. Gao, B. Xiao, T. Min, Y. Yang, S. Ma, and D. Yi, “The electronic, mechanical properties and theoretical hardness of chromium carbides by first-principles calculations,” *Journal of Alloys and Compounds*, vol. 509, no. 17, pp. 5242–5249, Apr. 28, 2011, ISSN: 0925-8388. DOI: 10.1016/j.jallcom.2011.02.009. Accessed: Jul. 14, 2024. [Online]. Available: <https://www.sciencedirect.com/science/article/pii/S0925838811003197>.
- [32] N. I. Medvedeva, D. C. Van Aken, and J. E. Medvedeva, “Stability of binary and ternary M23C6 carbides from first principles,” *Computational Materials Science*, vol. 96, pp. 159–164, Jan. 1, 2015, ISSN: 0927-0256. DOI: 10.1016/j.commatsci.2014.09.016. Accessed: Jul. 14, 2024. [Online]. Available: <https://www.sciencedirect.com/science/article/pii/S0927025614006272>.
- [33] M. Godec and D. A. Skobir Balantič, “Coarsening behaviour of M23C6 carbides in creep-resistant steel exposed to high temperatures,” *Scientific Reports*, vol. 6, no. 1, p. 29734, Jul. 13, 2016, ISSN: 2045-2322. DOI: 10.1038/srep29734. Accessed: Jul. 14, 2024. [Online]. Available: <https://www.nature.com/articles/srep29734>.
- [34] M. Mohammadnezhad, V. Javaheri, M. Shamanian, S. Rizane, and J. A. Szpunar, “Insight to the Microstructure Characterization of a HP Austenitic Heat Resistant Steel after Long-term Service Exposure,”
- [35] M. Wong-Kian, L. A. Cornisht, and A. van Bennekom, “Comparison of erosion-corrosion behaviour of hot isostatically pressed and welded stellite coatings,”
- [36] Š. Houdková, E. Smazalová, and Z. Pala, “Effect of Heat Treatment on the Microstructure and Properties of HVOF-Sprayed Co-Cr-W Coating,” *Journal of Thermal Spray Technology*, vol. 25, no. 3, pp. 546–557, Feb. 1, 2016, ISSN: 1544-1016. DOI: 10.1007/s11666-015-0365-5. Accessed: Jun. 8, 2025. [Online]. Available: <https://doi.org/10.1007/s11666-015-0365-5>.
- [37] R. Ahmed, H. L. de Villiers Lovelock, S. Davies, and N. H. Faisal, “Influence of Re-HIPing on the structure–property relationships of cobalt-based alloys,” *Tribology International*, vol. 57, pp. 8–21, Jan. 1, 2013, ISSN: 0301-679X. DOI: 10.1016/j.triboint.2012.06.025. Accessed: Jun. 30, 2024. [Online]. Available: <https://www.sciencedirect.com/science/article/pii/S0301679X12002241>.
- [38] H. Yu, R. Ahmed, and H. de Villiers Lovelock, “A Comparison of the Tribo-Mechanical Properties of a Wear Resistant Cobalt-Based Alloy Produced by Different Manufacturing

- Processes,” *Journal of Tribology*, vol. 129, no. 3, pp. 586–594, Jan. 9, 2007, ISSN: 0742-4787. DOI: [10.1115/1.2736450](https://doi.org/10.1115/1.2736450). Accessed: Nov. 17, 2024. [Online]. Available: <https://doi.org/10.1115/1.2736450>.
- [39] U. Malayoglu, A. Neville, and G. Beamson, “Characterisation of the passive film on HIPed Stellite 6 alloy using X-ray photoelectron spectroscopy,” *Materials Science and Engineering: A*, vol. 393, no. 1, pp. 91–101, Feb. 25, 2005, ISSN: 0921-5093. DOI: [10.1016/j.msea.2004.09.071](https://doi.org/10.1016/j.msea.2004.09.071). Accessed: Jun. 30, 2024. [Online]. Available: <https://www.sciencedirect.com/science/article/pii/S0921509304012511>.
- [40] K. C. Antony, “Wear-Resistant Cobalt-Base Alloys,” *JOM*, vol. 35, no. 2, pp. 52–60, 2 Feb. 1, 1983, ISSN: 1543-1851. DOI: [10.1007/BF03338205](https://doi.org/10.1007/BF03338205). Accessed: Jul. 13, 2024. [Online]. Available: <https://doi.org/10.1007/BF03338205>.
- [41] F. Pettit and G. Meier, “Oxidation and Hot Corrosion of Superalloys,” in *Superalloys 1984 (Fifth International Symposium)*, TMS, 1984, pp. 651–687. DOI: [10.7449/1984/Superalloys_1984_651_687](https://doi.org/10.7449/1984/Superalloys_1984_651_687). Accessed: May 17, 2025. [Online]. Available: http://www.tms.org/Superalloys/10.7449/1984/Superalloys_1984_651_687.pdf.
- [42] X. Z. Zhang, R. Liu, K. Y. Chen, and M. X. Yao, “Pitting Corrosion Characterization of Wrought Stellite Alloys in Green Death Solution with Immersion Test and Extreme Value Analysis Model,” *Journal of Materials Engineering and Performance*, vol. 23, no. 5, pp. 1718–1725, May 1, 2014, ISSN: 1544-1024. DOI: [10.1007/s11665-014-0952-5](https://doi.org/10.1007/s11665-014-0952-5). Accessed: May 17, 2025. [Online]. Available: <https://doi.org/10.1007/s11665-014-0952-5>.
- [43] K. Mohamed, M. Gad, A. Nassef, and A. El-Sayed, “Localized corrosion behaviour of powder metallurgy processed cobalt-base alloy Stellite-6 in chloride environments,” *Zeitschrift fuer Metallkunde/Materials Research and Advanced Techniques*, vol. 90, no. 3, pp. 195–201, 1999, ISSN: 0044-3093.
- [44] E. Lemaire and M. Le Calvar, “Evidence of tribocorrosion wear in pressurized water reactors,” *Wear*, vol. 249, no. 5, pp. 338–344, Jun. 1, 2001, ISSN: 0043-1648. DOI: [10.1016/S0043-1648\(00\)00544-5](https://doi.org/10.1016/S0043-1648(00)00544-5). Accessed: May 17, 2025. [Online]. Available: <https://www.sciencedirect.com/science/article/pii/S0043164800005445>.
- [45] J. Di Martino, C. Rapin, P. Berthod, R. Podor, and P. Steinmetz, “Corrosion of metals and alloys in molten glasses. Part 2: Nickel and cobalt high chromium superalloys behaviour and protection,” *Corrosion Science*, vol. 46, no. 8, pp. 1865–1881, Aug. 1, 2004, ISSN: 0010-938X. DOI: [10.1016/j.corsci.2003.10.025](https://doi.org/10.1016/j.corsci.2003.10.025). Accessed: May 17, 2025.

- [Online]. Available: <https://www.sciencedirect.com/science/article/pii/S0010938X03003081>.
- [46] A. Neville and U. Malayoglu, "3.06 - Aqueous Corrosion of Cobalt and its Alloys," in *Shreir's Corrosion*, B. Cottis, M. Graham, R. Lindsay, S. Lyon, T. Richardson, D. Scantlebury, and H. Stott, Eds., Oxford: Elsevier, Jan. 1, 2010, pp. 1916–1936, ISBN: 978-0-444-52787-5. DOI: [10.1016/B978-044452787-5.00093-7](https://doi.org/10.1016/B978-044452787-5.00093-7). Accessed: Jun. 8, 2025. [Online]. Available: <https://www.sciencedirect.com/science/article/pii/B9780444527875000937>.
- [47] R. Ahmed, V. Kumar, N. H. Faisal, M. Marri, and S. Davies, "Influence of Alloy Composition on the Tribomechanical Properties of 50% Blend of CoCrWMoCFeNiSiMn (Stellite 1) and CoCrMoCFeNiSiMn (Stellite 21) Alloys," *Journal of Materials Engineering and Performance*, Mar. 24, 2025, ISSN: 1544-1024. DOI: [10.1007/s11665-025-11034-7](https://doi.org/10.1007/s11665-025-11034-7). Accessed: Jun. 2, 2025. [Online]. Available: <https://doi.org/10.1007/s11665-025-11034-7>.
- [48] M. Sage and C. Guillaud, "Méthode d'analyse quantitative des variétés allotropiques du cobalt par les rayons X," *Revue de Métallurgie*, vol. 47, no. 2, pp. 139–145, 2 Feb. 1, 1950, ISSN: 0035-1563, 1156-3141. DOI: [10.1051/metal/195047020139](https://doi.org/10.1051/metal/195047020139). Accessed: Apr. 12, 2025. [Online]. Available: <https://www.metallurgical-research.org/articles/metal/abs/1950/02/metal19504702p139/metal19504702p139.html>.
- [49] R. P. Reed and R. E. Schramm, "Relationship between stacking-fault energy and x-ray measurements of stacking-fault probability and microstrain," *Journal of Applied Physics*, vol. 45, no. 11, pp. 4705–4711, Nov. 1, 1974, ISSN: 0021-8979. DOI: [10.1063/1.1663122](https://doi.org/10.1063/1.1663122). Accessed: May 30, 2025. [Online]. Available: <https://doi.org/10.1063/1.1663122>.
- [50] N. S. McIntyre, D. Zetaruk, and E. V. Murphy, "X-Ray photoelectron spectroscopic study of the aqueous oxidation of stellite-6 alloy," *Surface and Interface Analysis*, vol. 1, no. 4, pp. 105–110, 4 1979, ISSN: 1096-9918. DOI: [10.1002/sia.740010402](https://doi.org/10.1002/sia.740010402). Accessed: May 11, 2025. [Online]. Available: <https://onlinelibrary.wiley.com/doi/abs/10.1002/sia.740010402>.
- [51] Z. Česánek, J. Schubert, Š. Houdková, O. Bláhová, and M. Prantnerová, "Deterioration of Local Mechanical Properties of HVOF-Sprayed Stellite 6 after Exposure to High-Temperature Corrosion," *Key Engineering Materials*, vol. 662, pp. 115–118, 2015, ISSN: 1662-9795. DOI: [10.4028/www.scientific.net/KEM.662.115](https://doi.org/10.4028/www.scientific.net/KEM.662.115). Accessed: May 11, 2025. [Online]. Available: <https://www.scientific.net/KEM.662.115>.

- [52] C. J. Heathcock, A. Ball, and B. E. Protheroe, "Cavitation erosion of cobalt-based Stellite® alloys, cemented carbides and surface-treated low alloy steels," *Wear*, vol. 74, no. 1, pp. 11–26, Dec. 8, 1981, ISSN: 0043-1648. DOI: [10.1016/0043-1648\(81\)90191-5](https://doi.org/10.1016/0043-1648(81)90191-5). Accessed: May 17, 2025. [Online]. Available: <https://www.sciencedirect.com/science/article/pii/0043164881901915>.
- [53] "Cavitation Erosion," in *Fundamentals of Cavitation*, J.-P. Franc and J.-M. Michel, Eds., Dordrecht: Springer Netherlands, 2005, pp. 265–291, ISBN: 978-1-4020-2233-3. DOI: [10.1007/1-4020-2233-6_12](https://doi.org/10.1007/1-4020-2233-6_12). Accessed: Apr. 13, 2025. [Online]. Available: https://doi.org/10.1007/1-4020-2233-6_12.
- [54] S. Romo, J. Santa, J. Giraldo, and A. Toro, "Cavitation and high-velocity slurry erosion resistance of welded Stellite 6 alloy," *Tribology International*, vol. 47, pp. 16–24, 2012, ISSN: 0301679X (ISSN). DOI: [10.1016/j.triboint.2011.10.003](https://doi.org/10.1016/j.triboint.2011.10.003). [Online]. Available: <https://www.scopus.com/inward/record.uri?eid=2-s2.0-84856240362&doi=10.1016%2fj.triboint.2011.10.003&partnerID=40&md5=77bc5b529937543083c683cc6f5d689d>.
- [55] M. T. Gevari, T. Abbasiasl, S. Niazi, M. Ghorbani, and A. Koşar, "Direct and indirect thermal applications of hydrodynamic and acoustic cavitation: A review," *Applied Thermal Engineering*, vol. 171, p. 115 065, May 5, 2020, ISSN: 1359-4311. DOI: [10.1016/j.applthermaleng.2020.115065](https://doi.org/10.1016/j.applthermaleng.2020.115065). Accessed: Apr. 13, 2025. [Online]. Available: <https://www.sciencedirect.com/science/article/pii/S135943111937766X>.
- [56] Z. Huang, B. Wang, F. Liu, M. Song, S. Ni, and S. Liu, "Microstructure evolution, martensite transformation and mechanical properties of heat treated Co-Cr-Mo-W alloys by selective laser melting," *International Journal of Refractory Metals and Hard Materials*, vol. 113, p. 106 170, Jun. 1, 2023, ISSN: 0263-4368. DOI: [10.1016/j.ijrmhm.2023.106170](https://doi.org/10.1016/j.ijrmhm.2023.106170). Accessed: Apr. 13, 2025. [Online]. Available: <https://www.sciencedirect.com/science/article/pii/S0263436823000707>.
- [57] H. M. Tawancy, V. R. Ishwar, and B. E. Lewis, "On the fcc \rightarrow hcp transformation in a cobalt-base superalloy (Haynes alloy No. 25)," *Journal of Materials Science Letters*, vol. 5, no. 3, pp. 337–341, Mar. 1, 1986, ISSN: 1573-4811. DOI: [10.1007/BF01748098](https://doi.org/10.1007/BF01748098). Accessed: Apr. 13, 2025. [Online]. Available: <https://doi.org/10.1007/BF01748098>.
- [58] V. Stoica, R. Ahmed, and T. Itsukaichi, "Influence of heat-treatment on the sliding wear of thermal spray cermet coatings," *Surface and Coatings Technology*, vol. 199, no. 1, pp. 7–21, 2005, ISSN: 02578972 (ISSN). DOI: [10.1016/j.surfcoat.2005.03.026](https://doi.org/10.1016/j.surfcoat.2005.03.026). [Online]. Available: <https://www.scopus.com/inward/record.uri?eid=2-s2.0-21844464044&doi=10.1016%2fj.surfcoat.2005.03.026&partnerID=40&md5=6ad736723e828d39edf4a37c5975d2dc>.

- [59] M. Szala, D. Chocyk, A. Skic, M. Kamiński, W. Macek, and M. Turek, “Effect of Nitrogen Ion Implantation on the Cavitation Erosion Resistance and Cobalt-Based Solid Solution Phase Transformations of HIPed Stellite 6,” *Materials*, vol. 14, no. 9, p. 2324, 9 Jan. 2021, ISSN: 1996-1944. DOI: [10.3390/ma14092324](https://doi.org/10.3390/ma14092324). Accessed: May 30, 2025. [Online]. Available: <https://www.mdpi.com/1996-1944/14/9/2324>.
- [60] F. Rosalbino and G. Scavino, “Corrosion behaviour assessment of cast and HIPed Stellite 6 alloy in a chloride-containing environment,” *Electrochimica Acta*, vol. 111, pp. 656–662, Nov. 30, 2013, ISSN: 0013-4686. DOI: [10.1016/j.electacta.2013.08.019](https://doi.org/10.1016/j.electacta.2013.08.019). Accessed: Apr. 15, 2025. [Online]. Available: <https://www.sciencedirect.com/science/article/pii/S0013468613015338>.
- [61] N. Ogunlakin, A. S. Hakeem, S. H. Sohail, B. A. Ahmed, M. A. Ehsan, N. Ankah, and S. Ali, “Microstructural and Electrochemical Corrosion Characterization of a Novel 50 IN–50 Co Super Alloy Composite in 3.5wt.% NaCl Solution,” *Journal of Materials Engineering and Performance*, Mar. 6, 2025, ISSN: 1544-1024. DOI: [10.1007/s11665-025-10951-x](https://doi.org/10.1007/s11665-025-10951-x). Accessed: May 27, 2025. [Online]. Available: <https://doi.org/10.1007/s11665-025-10951-x>.
- [62] A. Karimi and W. R. Leo, “Phenomenological model for cavitation erosion rate computation,” *Materials Science and Engineering*, vol. 95, pp. 1–14, Nov. 1, 1987, ISSN: 0025-5416. DOI: [10.1016/0025-5416\(87\)90493-9](https://doi.org/10.1016/0025-5416(87)90493-9). Accessed: Aug. 1, 2024. [Online]. Available: <https://www.sciencedirect.com/science/article/pii/0025541687904939>.
- [63] J.-P. Franc, “Incubation Time and Cavitation Erosion Rate of Work-Hardening Materials,” *Journal of Fluids Engineering*, vol. 131, no. 2, Feb. 1, 2009, ISSN: 0098-2202, 1528-901X. DOI: [10.1115/1.3063646](https://doi.org/10.1115/1.3063646). Accessed: May 22, 2025. [Online]. Available: <https://asmedigitalcollection.asme.org/fluidsengineering/article/doi/10.1115/1.3063646/466754/Incubation-Time-and-Cavitation-Erosion-Rate-of>.
- [64] A. Thiruvengadam, “Theory of erosion,” *Proc. 2nd Meersburg Conf. on Rain Erosion and Allied Phenomena*, vol. 2, p. 53, Mar. 1, 1967.